Materials Science and Engineering B 302 (2024) 117261

Contents lists available at ScienceDirect

Materials Science & Engineering B

journal homepage: www.elsevier.com/locate/mseb

TiO_2-Fe_2O_3 nanocomposite thin films prepared by magnetron sputtering for photocatalytic applications

L. Escobar-Alarcón [a,*], D.A. Solis-Casados [b], S. Romero [a], E. Haro-Poniatowski [c]

[a] *Departamento de Física, Instituto Nacional de Investigaciones Nucleares, Carr. México-Toluca s/n La Marquesa, Ocoyoacac, Edo. de México C.P. 52750, Mexico*
[b] *Universidad Autónoma del Estado de México, Facultad de Química, Centro Conjunto de Investigación en Química Sustentable, UAEMex-UNAM, Paseo Colon esq. Paseo Tollocan S/N, CP 50120, Toluca, Estado de México, Mexico*
[c] *Departamento de Física, Universidad Autónoma Metropolitana Iztapalapa, Apdo. Postal 55-534, México City, Mexico*

ARTICLE INFO

Keywords:
Thin films
Magnetron sputtering
Titanium dioxide
Photocatalysis

ABSTRACT

The preparation and characterization of TiO_2-Fe_2O_3 nanocomposite thin films is reported. Films were deposited by magnetron sputtering using a multiple targets configuration to control the Fe content. The effect of the iron content in the films on the composition, structure and optical properties was investigated. With this experimental configuration, the iron was incorporated in a controlled way up to 23.5 at.%. X-ray diffraction and Raman results suggest that at low iron contents (<3.6 at.%) the obtained material consists of a mixture of the anatase and rutile phases of TiO_2 mainly whereas at higher iron concentrations (>17.3 at.%) nanocomposites formed by the rutile and hematite phases are obtained. The prepared films showed enhanced photocatalytic response for the Malachite Green dye degradation under irradiation with visible light compared with TiO_2 films being in some cases even better than Degussa P-25 powders.

1. Introduction

It is well known that TiO_2 under irradiation with UV and in some cases visible light can degrade, in several cases completely, many organic compounds. This is because the interaction of light with a semiconductor results in the formation of electron-hole pairs, which through different routes can generate strongly oxidizing species as the hydroxyl ($OH^{\bullet}$) radicals. In presence of air, the photoelectron reduces the oxygen molecules into the superoxide radical ($O_2^{\bullet}$), which through several steps can produce the $OH^{\bullet}$ radical. Similarly, in presence of water the hole oxidizes the H_2O molecule producing directly $OH^{\bullet}$ radicals. This is the base of photocatalysis, an advanced oxidation process, to decompose persistent organic molecules towards CO_2 and water, which are innocuous for human health. Among the semiconductors investigated for this purpose, the TiO_2 is considered as the archetypal photocatalyst, becoming a synonym of photocatalyst due to its good photocatalytic response, high stability under light irradiation, non-toxicity, low cost, accessibility, not soluble in liquid media and high oxidant power to mention just a few of its advantages. TiO_2 is found mainly in three crystalline polymorphs, anatase (tetragonal), rutile (tetragonal) and brookite (orthorhombic), the first two are the most used as photocatalysts [1]. In spite of its advantages, the use of TiO_2 as photocatalyst has an important drawback due to its wide band gap, 3.2 eV for the anatase phase, it can produce electron-hole pairs only under irradiation with wavelengths lower than 387 nm (UV light), which means that it absorbs only a little fraction (3–5 %) of the sunlight spectrum [2]. Clearly, the use of sunlight to activate photocatalysts convey many advantages, mainly because its abundance and inexpensiveness. Therefore, in recent years many efforts have been focused to develop photocatalysts that absorb wavelengths longer than 400 nm in the visible region of the electromagnetic spectrum [3–5].

Although there is an increasing interest in investigating other semiconductors as alternatives to TiO_2, this constitutes the benchmark in photocatalytic processes. Many efforts have been done to improve the photocatalytic activity of titania; among the strategies investigated for this purpose, doping with metals and non-metals, as well as its coupling with a second semiconductor, have been considered as good alternatives to develop high efficiency photocatalytic materials by inducing synergistic effects leading to the bandgap narrowing as well as promoting charge separation decreasing the recombination processes of the photoinduced charge carriers [6,7].

Particularly, the iron-doped TiO_2 or mixtures of Ti-Fe oxides have been reported to be photoactive with visible light [8]. Additionally, the Fe-doped titania has the advantage of reusability and recoverability for

---

* Corresponding author.
E-mail address: luis.escobar@inin.gob.mx (L. Escobar-Alarcón).

https://doi.org/10.1016/j.mseb.2024.117261
Received 18 September 2023; Received in revised form 25 January 2024; Accepted 16 February 2024

large scale industrial applications [9]. Among iron oxides, α-Fe_2O_3 (hematite) has a band gap around 2.2 eV [10], absorbing wavelengths lower than 620 nm, which represent a significant fraction of the solar spectrum, making it good photocatalytic material active with solar light. Additionally, both oxides (TiO_2 and α-Fe_2O_3) have good properties for this purpose such as chemical stability in aqueous environment, non-toxicity and low cost [11,12]. However, these oxides have an important disadvantage as photocatalysts, their very short diffusion length of photogenerated holes which increases the recombination rate and consequently diminishes their photocatalytic response [13]. To overcome this problem two approaches can be explored: first, combine TiO_2 and α-Fe_2O_3 producing nanocomposites to decrease the recombination rate of photogenerated electrons and holes, and at the same time narrowing the band gap; second, using nanostructured thin films allowing to reduce the depth where the electron-holes pairs are produced and consequently decreasing their recombination rate. The development of TiO_2-Fe_2O_3 nanocomposites with enhanced photocatalytic performance using visible light for the degradation of organic molecules has drawn the interest of researchers in the last years [14–20].

Therefore, the development of TiO_2-Fe_2O_3 nanocomposites in thin film form is of great interest due to their potential applications in the degradation of organic molecules present in wastewaters. It is worth mentioning that the use of photocatalyst in thin film form has important advantages such as an easy recovery from the treated solution, it also can prevent the scattering of light due to suspended particles and enhance the transmittance of light resulting in higher photoreaction efficiency [21].

The magnetron sputtering technique is a widely used Physical Vapor Deposition method to prepare thin films. Among the main advantages of this technique are a high deposition rate, good lateral and in-depth uniformity, as well as good control of the properties of the deposited films through an easy variation of deposition parameters such as power, working pressure, target to substrate distance and deposition rate, which allows to obtain films with tailored properties [22]. Sputtering is considered a very powerful and versatile technique suitable for the synthesis of new nanocomposites which can be used in a wide range of potential applications. Thin films of iron oxide and titanium oxide prepared by co-sputtering of iron and titanium targets and their subsequent oxidation has been reported [23]. The aim of this work is to show the obtained results using a multitarget deposition configuration to prepare TiO_2-Fe_2O_3 nanocomposite thin films with different amounts of Fe_2O_3 depending on the Fe content as well as to explore its capabilities to synthesize nanocomposites with good photocatalytic properties. In this line, our research group has been working in the implementation of different experimental techniques to develop nanomaterials with photocatalytic response under solar irradiation modifying the TiO_2 with different elements as Co [24], Ni [25] and Bi [26] among others. It is worth mentioning that the development of photocatalysts in thin film form requires still much work, in particular, to investigate alternative deposition techniques capable to produce nanomaterials with good photocatalytic response using solar light with the advantages that this implies.

2. Experimental

Titanium thin films with different amounts of iron were deposited onto glass substrates using a DC magnetron sputtering system (INTERCOVAMEX). To vary the iron content, a multiple targets configuration was implemented. A different number of Fe targets, each one with a 0.22″ diameter × 0.11″ thick were placed symmetrically onto the circular race-track produced by the Ar ion erosion on the Ti target (2″ diameter × 0.25″ thick) as is shown schematically in Fig. 1. The sputtered area reported for the titanium target corresponds to the area of the race-track whereas the sputtered area of each Fe target corresponds to their geometrical area; the Fe target diameter is lower than the width of the race-track. Each Fe target has a sputtered area of 25.6 mm^2 whereas the Ti target has a maximum sputtered area of 457 mm^2. The experimental variable was the ratio of sputtered areas of Fe to Ti (A_{Fe}/A_{Ti}) which was varied from 0 to 0.28. Sputtering was produced using argon ions, generating the plasma at a working pressure of 1.8×10^{-2} Torr applying a DC power of 100 W. The substrate was placed parallel to the target at 9.5 cm from the target surface in an on-axis configuration; the substrate temperature was close to 30 °C during deposition only 10 °C higher than the room temperature. Deposition time was 30 min for all deposits. In order to obtain titanium dioxide, the as-deposited thin films were subjected to thermal treatments in a muffle open to the atmosphere at temperatures of 200, 300, 400, 500, 550 and 600 °C to determine the optimal temperature to obtain TiO_2, which was established in 550 °C. Therefore, the reported results correspond to the samples subjected to a thermal treatment at 550 °C for 2 h. The effect of iron loading incorporated in the films on the composition, structure, optical properties, surface morphology and photocatalytic response was investigated for each sample.

Compositional characterization was performed using three different techniques: the first one was Energy Dispersive Spectroscopy (EDS) using an EDS probe (Oxford EDS-7274) attached to a scanning electron microscope (JEOL, JSM-5900LV); the second one was X-ray Photoelectron spectroscopy (XPS) with a K-Alpha ThermoScientific spectrometer, the XPS Spectra were acquired in the low and high-resolution regimes with an Al-Kα X-ray source; the third one was the Rutherford Backscattering Spectroscopy (RBS), in this case, a 12.0 MeV C^{2+} ion beam from a Tandem Van de Graff accelerator at a backscattering angle of 165° was used. Structural characterization was carried out by micro-Raman Spectroscopy and X-Ray Diffraction (XRD); Raman measurements were carried out using a micro-Raman system (HR LabRam 800) with a Nd:YAG laser ($\lambda = 532$ nm) in the backscattering configuration, XRD patterns were obtained using a Bruker AXS D8-Discover diffractometer with the Cu K_α radiation ($\lambda = 1.5406$ Å). The optical properties were determined from UV–Vis (Perkin Elmer lambda 35) and photoluminescence (PL) measurements (FluoroMax 4, Horiba Jobin Yvon). The deposited films were evaluated in the degradation of the Malachite Green dye under simulated solar light (SF150 of Sciencetech solar simulator) at a power density close to 30 mW/cm^2 to assess their photocatalytic response to visible radiation.

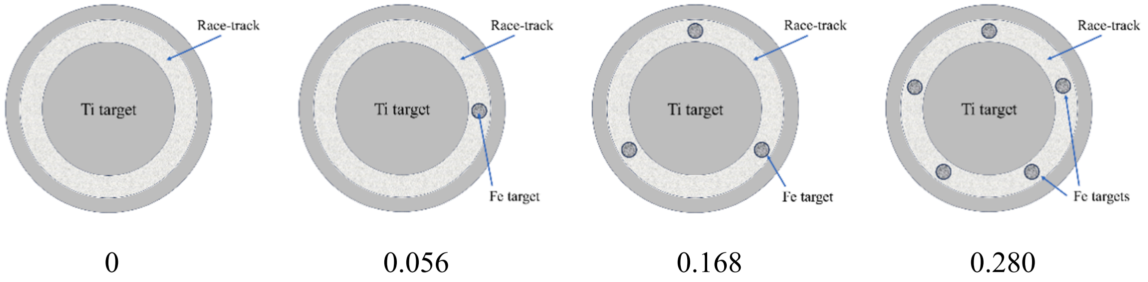

Fig. 1. Schematic arrangement of three multitarget configurations and the corresponding ratio of sputtered areas.

3. Results and discussion

In general terms, the as-deposited titanium thin films exhibit a metallic appearance becoming semi-transparent as result of the thermal treatment; this change is expected due to the Ti oxidation and the subsequent TiO_{2-x} formation.

3.1. Compositional characterization

The EDS measurements were carried out at various positions in each film reporting the average of 5 measurements. Fig. 2 shows the evolution of the atomic content of oxygen and titanium in the thin films as a function of the thermal treatment temperature. As it is seen for the films treated at 200 and 300 °C the O/Ti ratio is approximately 1 indicating that at these temperatures the titanium film is oxidized forming TiO. When the temperature is increased from 300 °C up to 500 °C, it is clearly observed that the oxygen atomic concentration increases from 52 to 64 at.% respectively. At the same time the titanium atomic concentration decreases from 48 to 36 at.%. These results suggest that a sub-stoichiometric titanium dioxide was obtained at 500 °C. For annealing temperatures greater than 500 °C, the atomic concentration of each element remains almost constant with an O/Ti ratio of 1.9, very close to the stoichiometric value corresponding to TiO_2. The horizontal lines in Fig. 1, indicate the at.% values corresponding to Ti and O in TiO_2 as reference. Based on these results all the samples were thermally treated at 550 °C in order to obtain titanium dioxide thin films.

EDS measurements were carried out again at several points in the films with different iron content. Table 1 and Fig. 3 show the composition of the films as a function of the A_{Fe}/A_{Ti} ratio. Measurements show that films without Fe and those prepared using an A_{Fe}/A_{Ti} ratio of 0.03 correspond to sub-stoichiometric titanium dioxide (TiO_{2-x}). Fig. 3 shows the Fe content in the films as a function of the ratio of sputtered areas (A_{Fe}/A_{Ti}), the monotonous behavior observed indicates that the A_{Fe}/A_{Ti} ratio can be used to vary the amount of iron incorporated in the film in a controlled way from 0 up to 23.5 at.%.

In order to obtain information about the chemical environment and the oxidation state of the elements present in the films, these were characterized by XPS. The adventitious carbon peak at 284.8 eV (C-1 s) was used as the internal standard to calibrate the XPS spectra. In Fig. 4 the XPS high-resolution spectra of the binding energy regions of interest are shown: (a) Fe-2p, (b) Ti-2p, and (c) O-1s, corresponding to the sample with a Fe content of 17.3 at.% at different etching times: 90, 600 and 1200 sec. The spectra of the Fe-2p3/2 region (Fig. 4a) shows a peak centered at 709.9 eV for erosion times of 90 and 600 sec, this peak can be attributed to Fe^{3+} in Fe_2O_3 [27]; for an erosion time of 1200 sec, additionally to the peak at 709.9 eV a shoulder appears at 706.7 eV attributed to metallic Fe^0 [28], in this case, in a deeper region of the thin film, there is a mixture of Fe_2O_3 and Fe^0 inside the film. Two signals peaking at 458.5 and 464.5 eV, are observed in the Ti-2p region (Fig. 4b), attributed to Ti-2p3/2 and Ti-2p1/2 respectively of TiO_2 in its anatase phase [29]. From Fig. 4a and 4b it is clearly seen that the intensity of the signal due to Fe decreases whereas the signal intensity of Ti increases as the etching time increases, that is, as the erosion depth become greater indicating a concentration gradient in opposite directions of Fe and Ti along the film thickness. Fig. 4c shows the convolutional fitting spectrum of the Ti-2p region. Results reveal the existence of 4 doublets, the most intense with peaks at 458.0 and 464.0 eV corresponding to the Ti 2p3/2 and Ti 2p1/2 orbitals respectively, these can be assigned to Ti^{4+} in the TiO_2 lattice in its anatase crystalline phase; the second doublet at higher binding energies at 459.2 and 465.4 eV can be assigned to Ti^{4+} state in the TiO_2 lattice in its rutile crystalline phase [30]. The third doublet peaking at 456.6 and 462.5 eV can be assigned to the Ti^{3+} in the Ti_2O_3 [31], whereas the fourth one at 455.5 and 460.9 eV is characteristic of Ti^0 in metallic Ti [32]. These last two doublets appear due to the oxygen deficiency in TiO_2 caused by a chemical reduction effect due to preferential sputtering of O by the Ar ions used for etching, promoting the reduction of TiO_2 to Ti_2O_3 and metallic Ti [33].

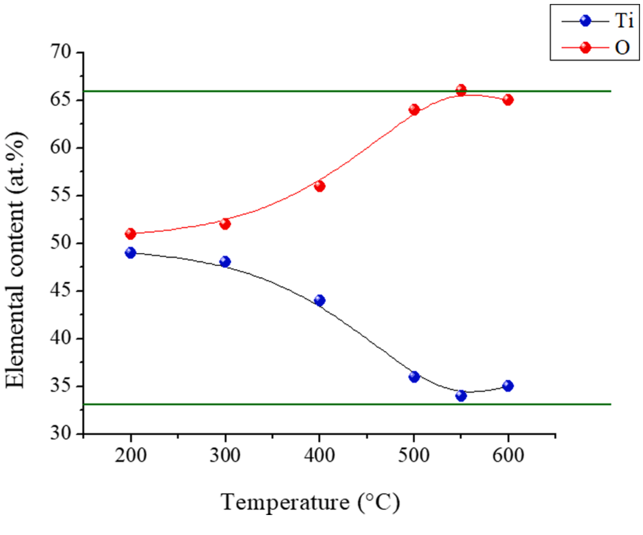

Fig. 2. Thin film composition as a function of the thermal treatment temperature.

Table 1
Composition of the films as a function of the A_{Fe}/A_{Ti} ratio.

A_{Fe}/A_{Ti}	Fe (at.%)	Ti (at.%)	O (at.%)
0	0	35.0	65.0
0.03	3.6	33.6	62.8
0.07	6.1	28.4	65.5
0.10	12.2	24.8	63.0
0.17	17.3	20.7	62.0
0.28	23.5	12.7	63.8

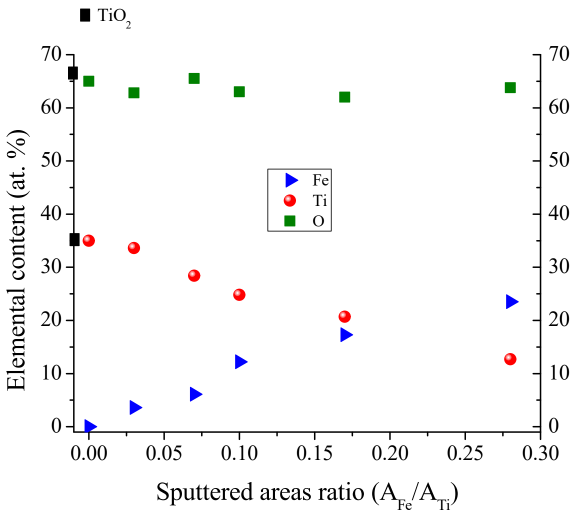

Fig. 3. Elemental content as a function of the sputtered areas ratio.

The high resolution XPS spectra of the O-1s region are shown in Fig. 4d. For 90 and 600 sec of etching time a symmetric peak centered around 529.4 eV corresponding to O-1s in Fe_2O_3 is observed, whereas at 1200 sec of etching time a shift to higher binding energies indicating a change of chemical state is clearly observed, in this case the peak at 529.6 eV is attributed to TiO_2.

In order to gain better insight about the distribution of Ti and Fe in the film, XPS depth profiles of these elements for different films were

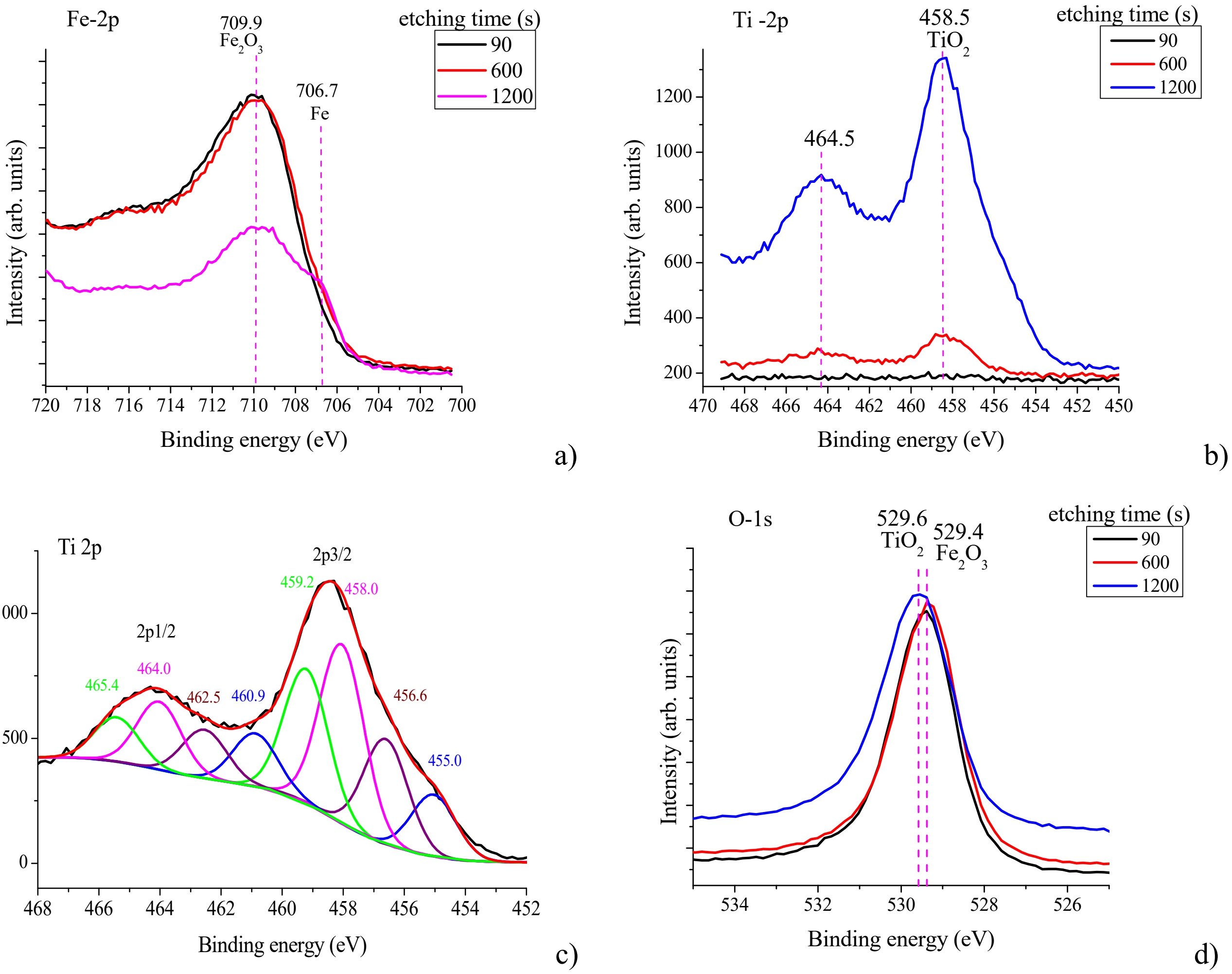

Fig. 4. High resolution XPS spectra of the (a) Fe-2p3/2, (b) Ti-2p, (c) Ti2p spectrum deconvolution of the sample after 1200 sec of etching and (d) O-1s, of the film with 17.3 at.% of Fe.

obtained and shown in Fig. 5. As the Fe content increases a thicker layer of iron is formed on the film surface whereas the titanium appears at deeper depths shifting towards the substrate. This result reveals a segregation process resulting in a bilayer in which a Fe rich layer appears on the top whereas a Ti rich layer is formed below onto the substrate surface. Another feature observed in these profiles reveals gradients of concentration of Fe and Ti indicating a region in which a mixture of these elements is present.

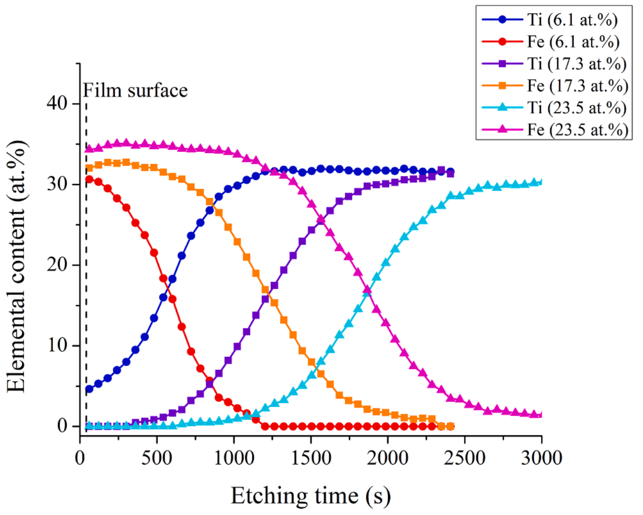

Fig. 5. XPS depth profiles of Ti and Fe of films with different Fe content.

These results were verified through RBS measurements shown in Fig. 6a. The RBS spectrum of the sample without Fe (at the bottom in black) shows the signal due to Ti with the leading edge close to the channel 1440 corresponding to titanium atoms on the film surface. The almost constant plateau of this profile indicates an uniform distribution of Ti along the thickness of the film. As the iron content increases a shift of the leading edge to lower channel number is clearly observed. The leading edge close to the channel 1515 corresponding to iron atoms on the film surface is observed. As the Fe content increases the profile of this signal becomes wider indicating a thicker layer of Fe on the top of the film. These results reveal the formation of a bilayer with the Fe_2O_3 film on the top and a TiO_2 film below as is shown schematically in Fig. 6b for each spectrum.

A more detailed analysis of the RBS spectrum of the sample with 6.1 at.% of iron was carried out showing a lower slope of the trailing edge of the Fe profile and of the leading edge of the Ti profile indicative of segregation of these two elements. The simulation results of this spectrum, using a code developed in our laboratory, considering three layers are shown in Fig. 7. A Fe_2O_3 layer with a mass thickness of 30 $\mu g/cm^2$ on top followed by an intermixed layer of 40 $\mu g/cm^2$ and a TiO_2 layer of 90 $\mu g/cm^2$ at the bottom. Taking into account that the deposited TiFe film was subjected to thermal treatment in air at 550 °C for 2 h, this treatment, in addition to produce oxidation and crystallization of the TiFe

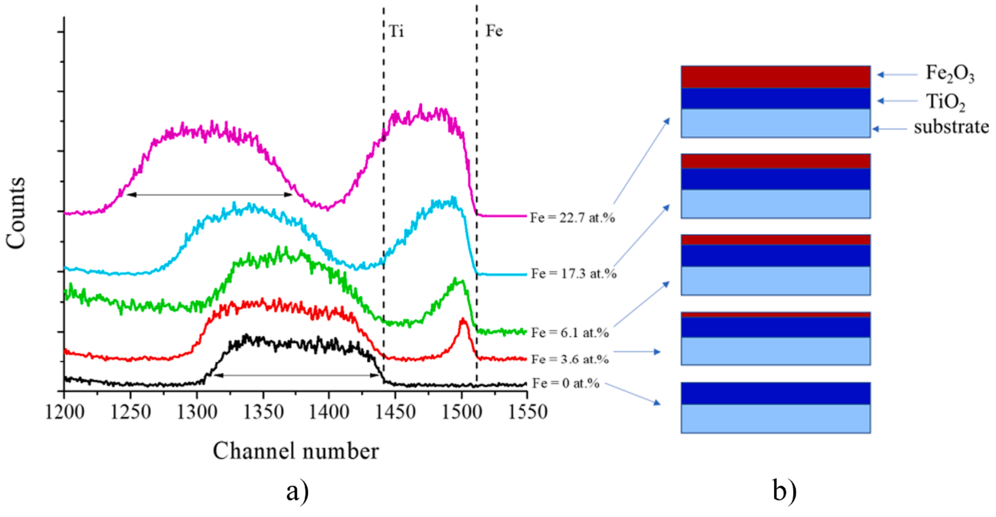

Fig. 6. (a) RBS spectra of films with different Fe content and (b) schematic of the bilayers formed.

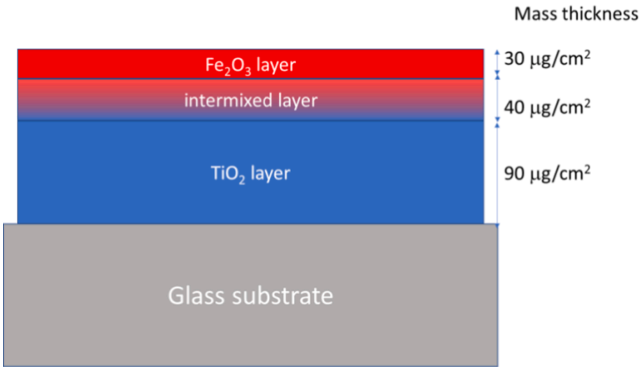

Fig. 7. Schematic drawing showing the tri-layer system resulting of the RBS simulation.

system, provoked the thermally induced phase separation observed. Such behavior has been observed in the system TiZn subjected to the same conditions as the previous one [34]. In both cases, we suppose that the positive enthalpy of mixing of these systems is the fundamental cause of phase separation; several reports support this interpretation [23,35,36]. It must be pointed out that the underlying mechanisms of the segregation effect observed are still under investigation.

3.2. Structural characterization

Structural characterization results reveal that films without thermal treatment were amorphous whereas the films thermally treated at 550 °C crystallize differently depending on the iron content. Fig. 8 shows the Raman spectra of samples with different Fe load after the thermal treatment. The Raman spectrum of the sample without iron presents peaks at 143, 198, 399, 517 and 638 cm^{-1} characteristics of the anatase phase of TiO_2, additional peaks are observed at 240, 442 and 609 cm^{-1} corresponding to the rutile phase of TiO_2 [37] indicating that a mixture anatase–rutile is present. The presence of the rutile phase at this temperature can be attributed to the fact that magnetron sputtering involves energetic species which provide additional non-thermal energy during film growth due to a higher surface mobility promoting the anatase to rutile phase transition occurrence at lower temperatures. The film with 3.6 at.% of iron shows peaks at 143, 393, 512 and 637 cm^{-1} as well as at 442 and 610 cm^{-1} corresponding to the mixture anatase–rutile, additionally, new peaks at 225, 245, 291, 298, 411 and 659 cm^{-1} are observed. These new signals are indicative of the formation of iron oxide [38]. At the iron content of 6.1 at.% more intense peaks, suggesting an improvement of crystallinity, are observed; the Raman features of TiO_2 at 142, 444, and 611 cm^{-1} remain, whereas the peaks attributed to iron oxide are now clearly observable. Raman spectra of samples with iron contents greater than 16.2 at.% are characterized by peaks at 221, 240, 286, 402, 493, 601 and 1308 cm^{-1} that agree very well with the hematite (α-Fe_2O_3) Raman features [39]. It is evident that as the Fe content increases the spectra are more intense. The spectra corresponding to the samples with iron contents greater than 17.3 at.% show still the peak at 143 cm^{-1} indicating the presence of the titania phase suggesting the formation of the TiO_2-Fe_2O_3 nanocomposite for iron contents greater than 3.6 at.%. The percentage of each titania phase in the mixture was determined following the procedure proposed by Clegg [40]; the obtained results shown in Table 2 reveal that as the iron content increases the amount of the Rutile phase increases as well, suggesting that Fe promotes the phase transition from Anatase to Rutile.

Fig. 9 shows the X-ray diffraction spectra of the different films. The sample without iron displays diffraction lines at 27.4, 36.1, 41.2 and 54.3° (labeled as R) attributed to the TiO_2 rutile phase (JCPDS 01-071-0650). Two weak signals at 25.3 and 37.8° (labeled as A) assigned to the anatase phase of TiO_2 (JCPDS 01-071-1166) are also observed. These results indicate a Rutile-Anatase mixture being the Rutile the predominant phase. At 3.6 at.% of iron, the peaks corresponding to Rutile become sharper and more intense suggesting and improved crystallinity of this phase. In this X-ray pattern a weak reflection at 30.0° (labeled as T) that could be attributed to the (220) plane of titanomagnetite, $Fe_{2.5}Ti_{0.5}O_4$ (JCPDS 01-075-1375), is also observed. At 6.1 at.%, besides the diffraction lines of the rutile and the titanomagnetite phase, new diffraction peaks close to 23.7, 32.5, 35.2, and 53.0° (labeled as I) that could be assigned to the (012), (104), (110) and (1 1 –6) planes of iron titanate ($Fe_{1.04}Ti_{0.96}O_3$) appear with very low intensity. Additionally, it is observed a decrease in crystallinity as the lower peak's intensity reveals. This could be attributed to distortion of the titania lattice due to the iron incorporation. Therefore, at this iron content, a mixture of rutile-titanomagnetite-iron titanate compose the film. The diffraction pattern of the film with 12.2 at.% of Fe shows reflections at 27.7, 33.4, 35.6, 36.4, 41.2, 49.5 and 54.3° (labeled as P); these can be attributed to the formation of the pseudorutile phase (JCPDS 01-013-0326) with the composition $Fe_2(TiO_3)_3$ and has been reported as a phase transition between ilmenite ($Fe_{1.04}Ti_{0.96}O_3$) and rutile (TiO_2) [41]. A further increase in the Fe content up to 17.3 at.%, results in strong and sharp diffraction peaks at $2\theta = 24.2$, 33.2, 35.7, 40.9, 49.5, 54.2 and 57.6° (labeled as H) corresponding to the α-Fe_2O_3 hematite phase (JCPDS 01-079-0007); a weak signal appears at 27.7° indicating that the

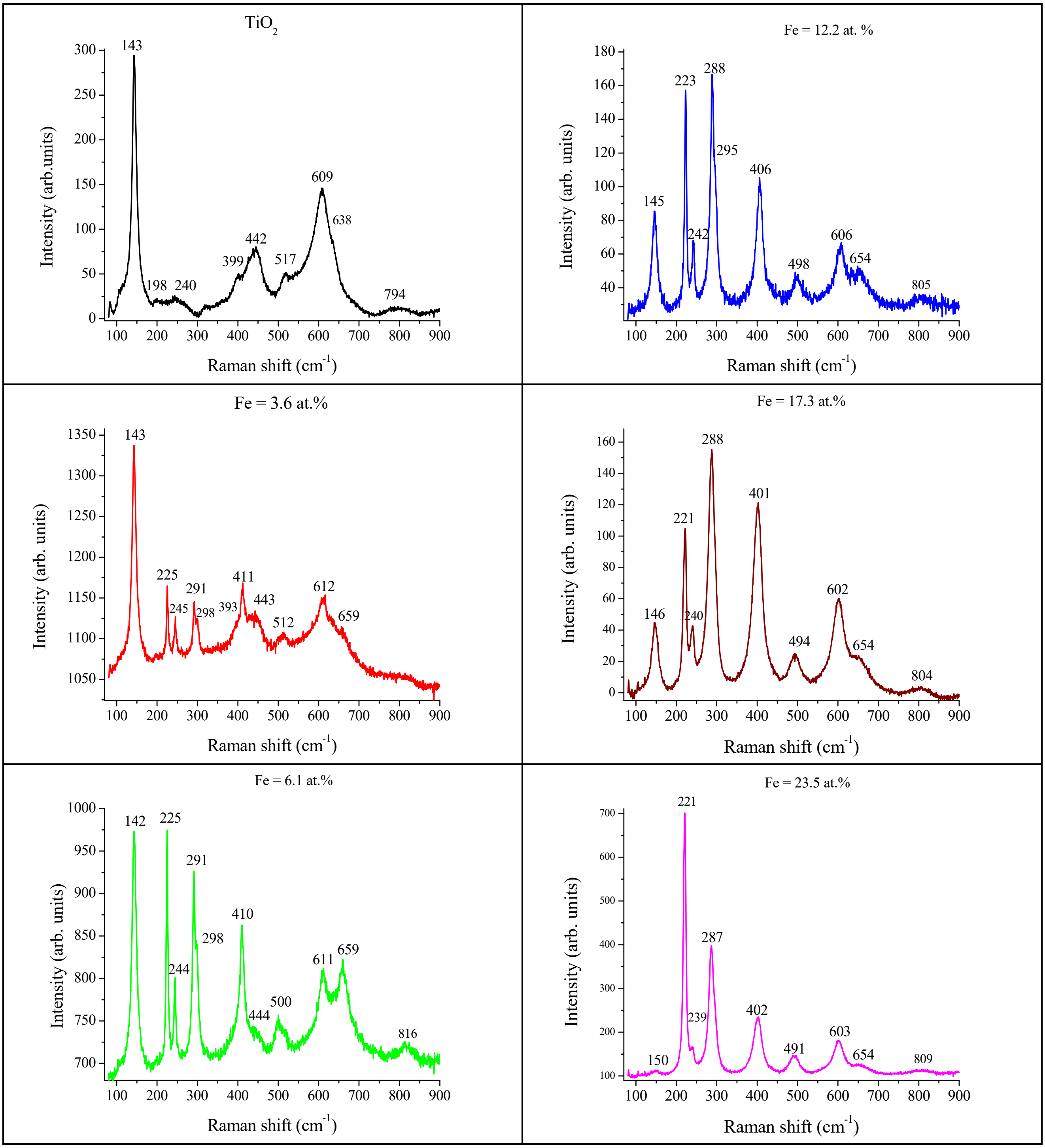

Fig. 8. Raman spectra of thin films with different iron content, from 0 to 23.5 at.%.

Table 2
Crystalline phases identified from XRD and Raman spectroscopy in the films with different Fe load.

Fe (at.%)	Phases present					
0	TiO_2 Rutile (82 %)	TiO_2 Anatase (18 %)				
3.6	TiO_2 Rutile (80 %)	TiO_2 Anatase (20 %)	$Fe_{2.5}Ti_{0.5}O_4$			
6.1	TiO_2 Rutile (87 %)	TiO_2 Anatase (13 %)	$Fe_{2.5}Ti_{0.5}O_4$	$Fe_{1.04}Ti_{0.96}O_3$		
12.2	TiO_2 Rutile (91 %)	TiO_2 Anatase (9 %)			$Fe_2(TiO_3)_3$	
17.3	TiO_2 Rutile (93 %)	TiO_2 Anatase (7 %)			$Fe_2(TiO_3)_3$	α-Fe_2O_3
23.5					$Fe_2(TiO_3)_3$	α-Fe_2O_3

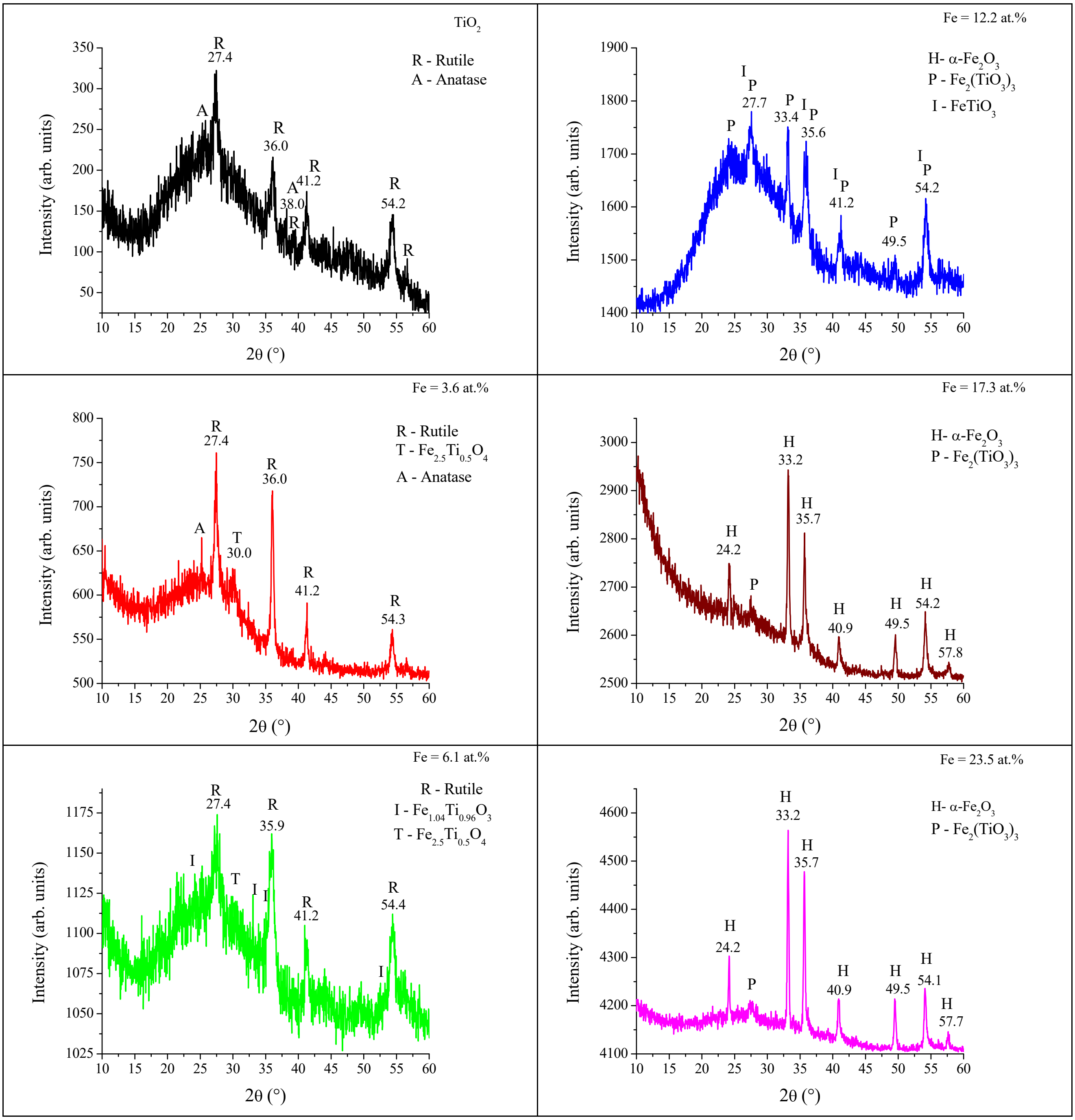

Fig. 9. XRD patterns of thin films with different iron content, from 0 to 23.5 at.%.

pseudorutile phase is still present. At the highest Fe content, 23.5 at.%, a very similar diffraction pattern, but with higher intensity, corresponding to the hematite phase was obtained. Table 2 shows a summary, obtained from the XRD and Raman results, of the phases present in the different films depending on the iron content. As it is seen, the TiO_2 phase is present in all the samples. Depending on the Fe load, mixtures of titania with different iron oxides compose the films being the dominating phases Rutile at low Fe loads and Hematite at higher Fe loads.

3.3. *Optical characterization*

Fig. 10 shows the transmittance spectra obtained by UV–Vis spectroscopy. As it can be observed, the incorporation of iron has an important effect on the position of the absorption edge which shifts towards longer wavelengths with increasing iron content. This indicates that films containing iron absorb a greater fraction of the visible region of the electromagnetic spectrum including wavelengths up to 570 nm. Additionally, the transmittance spectra show maxima and minima due to interference effects from which the refractive index and thickness can be determined approximately using the Goodman model [42]. For this purpose, the values of the maximum (T_{MAX}) and minimum (T_{MIN}) of interference are determined from the transmittance spectra. The Goodman model proposes that the refractive index of the film can be calculated using the following equation [42]:

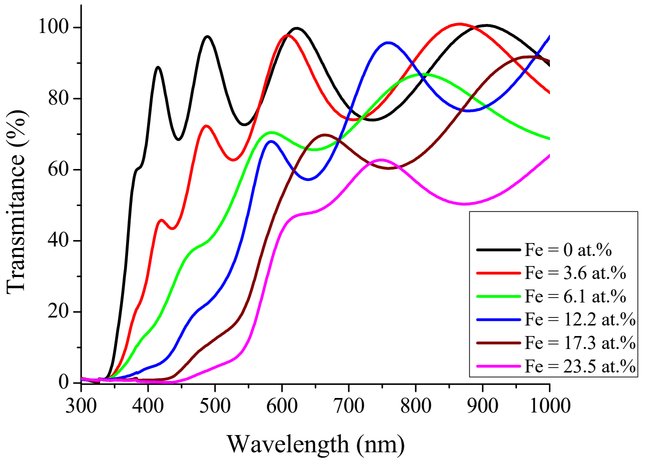

Fig. 10. Transmittance spectra of the different samples showing the effect of the Fe content.

$$n_p = \left\{ \frac{-\left(n_0^2+n_2^2\right)\left(1-2\rho_{T2}\right) + \left[\left(n_0^2+n_2^2\right)\left(1-2\rho_{T2}\right)^2 - 4n_0^2 + n_2^2\right]^{1/2}}{2} \right\}^{1/2}$$

Where:

n_p: refractive index of the thin film.

n_0: refractive index of air (1.0).

n_2: refractive index of the glass substrate (1.5).

and $\rho_{T2} = \frac{T_{MAX}}{T_{MIN}}$.

Once the refractive index of the thin film has been calculated, the thickness can be determined from the values of the wavelengths corresponding to the maximum and minimum of transmittance using the equation [42]:

$$t = \frac{M_{ab}\lambda_a\lambda_b}{2(\lambda_a - \lambda_b)\left(n_p^2 - \sin^2\theta_0\right)^{1/2}}$$

Where:

n_p: refractive index of the thin film.

λ_a: wavelength of maximum transmittance.

λ_b: wavelength of minimum transmittance.

M_{ab}: number of maxima or minima that separate λ_a from λ_b.

θ_0: angle of incidence of light (0°).

The obtained results reveal thicknesses from 476 to 676 nm, which in some cases were confirmed with profilometry measurements with a good agreement. Meanwhile, the index of refraction decreases from 2.23 to 1.89.

The band gap was determined using the Tauc method assuming direct transitions [43]. This was done by plotting $(\alpha E)^{1/2}$ as a function of the photon energy. The E_g values were obtained by a linear fit of the linear portion of the curve as the quotient of the intercept to the slope. Fig. 11 shows the $(\alpha E)^{1/2}$ versus E graphs as well as the linear fits and the E_g values obtained in each case. In general, good fits to the experimental curves were obtained. The obtained results are presented in Table 3 where it is seen that the sample without iron has a band gap energy of 3.1 eV. Incorporation and further increase of Fe content decreases the band gap to values as low as 1.7 eV.

The PL spectrum of the TiO_2 (black spectrum in Fig. 12) is characterized by a broad emission band from 350 to 550 nm attributed mainly to oxygen vacancies according to the elemental composition results. The maximum of emission, at 403 nm (3.08 eV), agrees very well with the band gap value and can be attributed to an interband transition. The PL emissions observed at 450, 470 and 567 nm can be attributed to excitonic PL emission due to the surface states of oxygen vacancies in TiO_2 in its anatase phase [44]. A strong quenching of the PL emission at 407 nm due to Iron incorporation in the thin film is observed as well as an increase in intensity of the emissions at longer wavelengths caused by a decrease in the band gap originated from structural defects created inside the gap. Additionally, the intensity of the peak around 569 nm increases, reaching its maximum at a Fe load of 6.1 at.%, indicating an increase in the number of oxygen vacancies.

These results show that PL emission strongly depends on the Fe content. Additionally, this behavior shows that PL efficiency decreases with decreasing optical gap and the PL spectra are red-shifted consistent with previous reports [45]. At the highest Fe contents, a new emission peaking at 615 nm (2.01 eV) is clearly observed, revealing the presence of new levels of energy. This emission can be assigned to the band gap transition of α-Fe_2O_3 [46] whose reported value is close to 2.1 eV. Clearly, these new levels are responsible for the band gap change due to the Fe incorporation.

3.4. Morphological characterization

The AFM analysis reveal differences in the surface morphology of the films with different Fe content as is shown in Fig. 13. The TiO_2 film, without iron, shows a homogeneous surface morphology with only slight roughness and without evidence of granular structure. On the contrary, the surface morphology is significantly changed when Fe is incorporated into the film. As the Fe content increases, the formation of granular structures with increasing size is observed. This is indicative of a coalescence process followed by the formation of granular structures thus increasing the roughness of the film. This is a typical behavior of crystalline or quasicrystalline materials, suggesting that the structure became increasingly ordered in good agreement with XRD results. Additionally, this increased roughness of the film could be responsible for the decrease in the intensity of the photoluminescent response because a lower number of defects.

3.5. Photocatalytic activity

As first step for the photocatalytic response measurements, the relation of the absorbance as a function of the Malachite Green dye concentration was determined. The intensity of the characteristic absorbance band of MG, peaking at 620 nm, was measured by UV–Vis spectroscopy for solutions with different known MG concentrations. In this way a calibration curve is obtained. The obtained results followed a linear relation, and a linear fitting was used to determine the MG concentration as function of the absorbance. The photocatalytic reaction system consists of 25 mL of the malachite green (MG) solution in which the thin film is introduced. The reaction system was kept in dark to reach equilibrium adsorption between the solution and the photocatalyst. Afterwards, the thin film was irradiated using a solar light simulator, taking aliquots to measure the absorbance at different irradiation times. The MG degradation was determined correlating the absorbance values at each time to MG concentrations using the calibration curve previously determined. Fig. 14 shows the change in intensity of the absorption band depending on the irradiation time corresponding to the sample with a Fe content of 6.1 at.% which showed the highest photocatalytic response. A clear intensity decrease as the irradiation time increases is observable suggesting the degradation of the dye molecule.

Fig. 15 shows the degree of MG degradation as a function of the reaction time. It is observed that the TiO_2 film degrade around 21 % after 120 min. Further increase of the Fe content from 3.6 to 16.2 at.%, improves the photocatalytic activity reaching approximately 45 % for the sample with 6.1 at.% of iron. This attained degradation degree is 100 % better than the response of the TiO_2 film without Fe. The enhanced photocatalytic response at this iron content could be attributed to the fact that this sample is composed by a mixture of the titania crystalline phases, anatase and rutile, as well as hematite, according to the Raman spectroscopy results presented before. These phases can behave as coupled semiconductors promoting the charge transfer

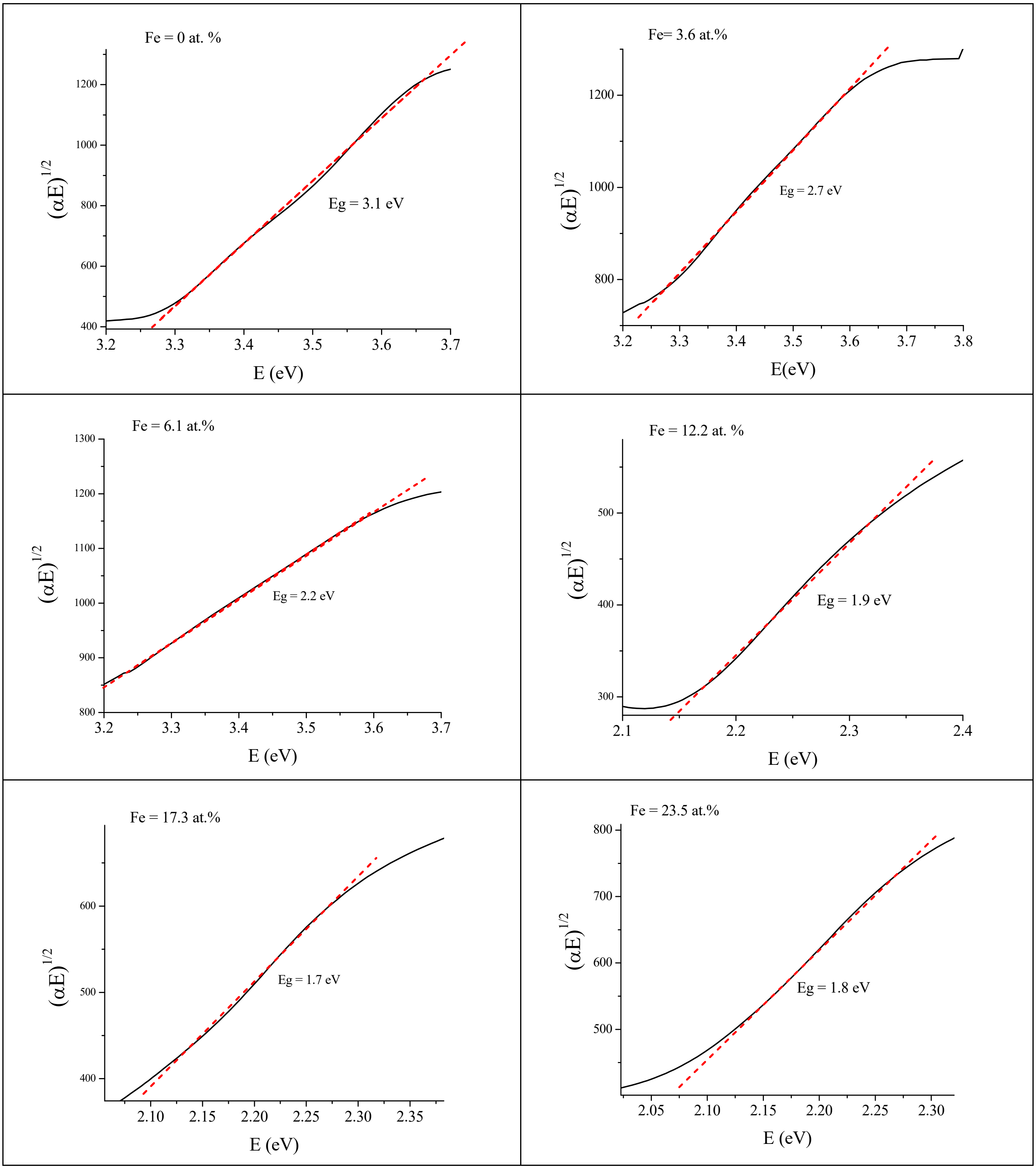

Fig. 11. Tauc plots as well as the linear fits and the E_g values obtained in for films with different Fe load.

between their conduction bands and thus inhibiting the photoinduced electron-hole pair recombination rate as the PL measurements reveal and consequently enhancing the photocatalytic activity. The samples with higher Fe contents i.e. greater than 17.3 at.%, show lower degradation degrees than the obtained for the film without iron. It is worth mentioning that according to the PL characterization, the excitonic PL emission for the film with 6.1 at% of Fe is higher than for films containing 3.6, 12.2 and 17.3 at% of Fe. It has been reported that the increase of defects and oxygen vacancies at the thin film surface can produce higher photoluminescence intensity due to excitonic PL processes and higher photocatalytic activity [47]. This is attributed to a strong interaction between the photo-induced electrons bound by oxygen vacancies and the adsorbed O_2 producing the superoxide radical which explain the correlation of surface oxygen vacancies with photoluminescence and the photocatalytic activity [48].

It seems that the degradation values reached are low; however, it must be considered that the mass of the thin film employed as photocatalyst, estimated from RBS measurements, is around 150–200 μgrs.

Table 3
Band gap, thickness, and refractive index of the samples with different iron content.

Fe (at.%)	E_g (eV)	Thickness (nm)	n
0	3.1	514	2.23
3.6	2.7	476	2.20
6.1	2.2	569	2.18
12.2	1.9	655	2.07
17.3	1.7	667	1.89
23.5	1.8	620	2.08

These values agree well with the density values reported previously for TiO_2 thin films [49].

In an attempt to gain insight about the photocatalysis mechanism involved in the degradation process of the MG dye, experiments using two photocatalysts, with iron contents of 3.6 and 6.1 at.%, in presence of scavenger molecules were performed. The p-Benzoquinone (BZQ) molecule was used to block the superoxide radicals (O_2•); triethanolamine (TEOA) was used to block the holes (h^+) and 2-propanol (IPA) was added to block the hydroxyl radicals (OH•) [50]. Fig. 16 shows the kinetic rate constants determined in each case. The results show that the kinetic rate constants are very low when IPA and BZQ are used. This indicates that holes (h^+) and OH• radicals practically do not contribute

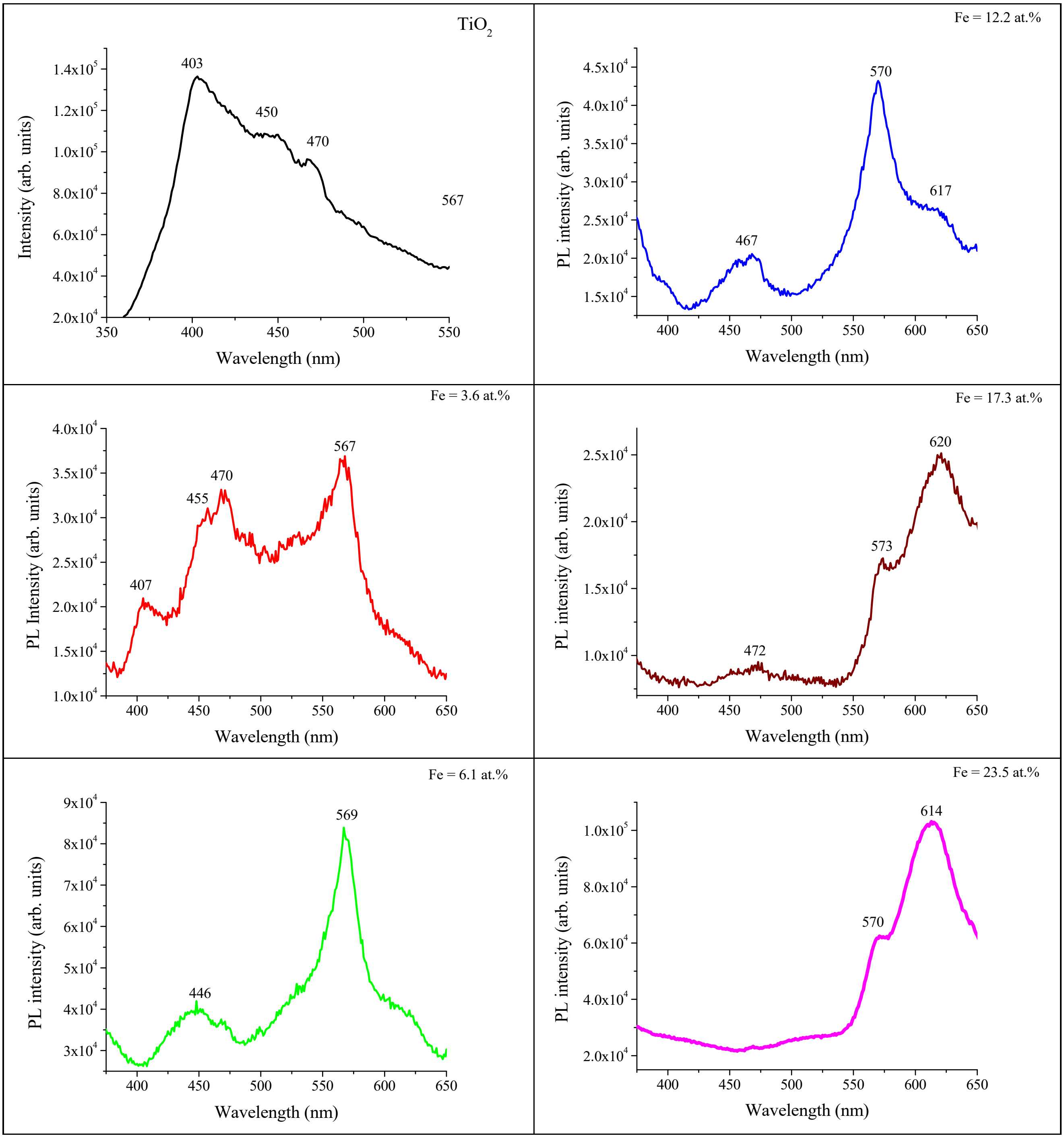

Fig. 12. PL spectra of the different samples showing the effect of the Fe content.

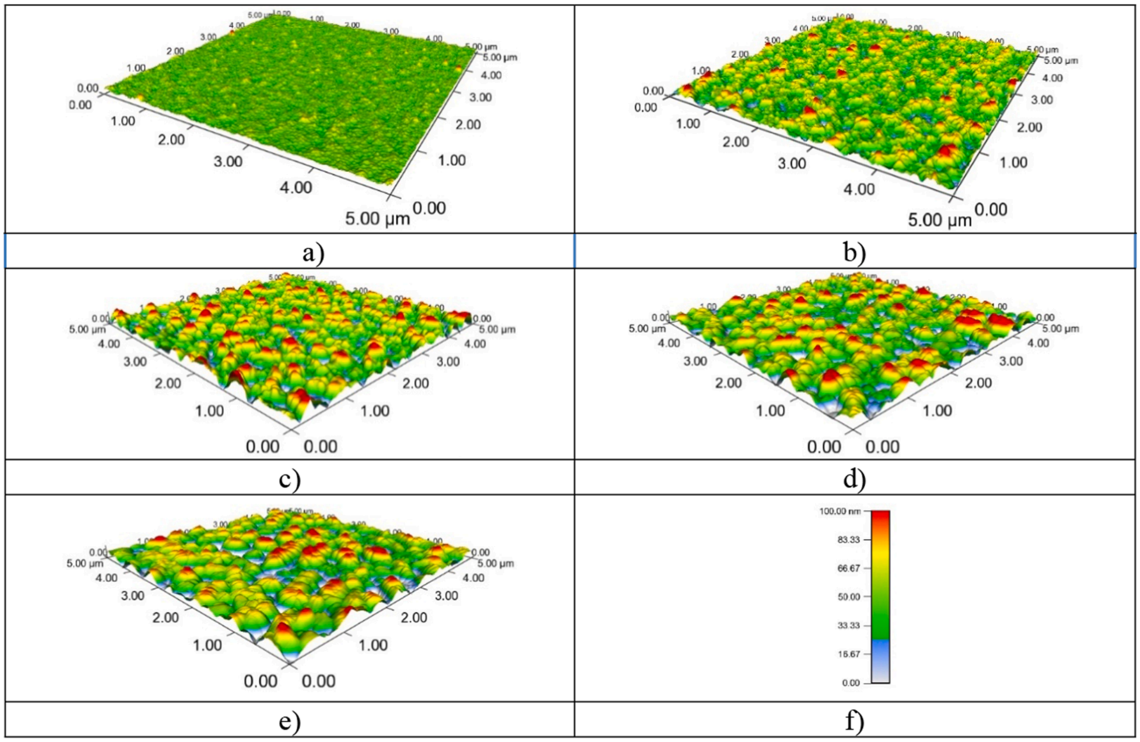

Fig. 13. Topography AFM images of films with different Fe content (a) 0 at.%, (b) 3.6 at.%, (c) 6.1 at.%, (d) 12.2 at.%, (e) 17.3 at.%, (f) height scale of the AFM images.

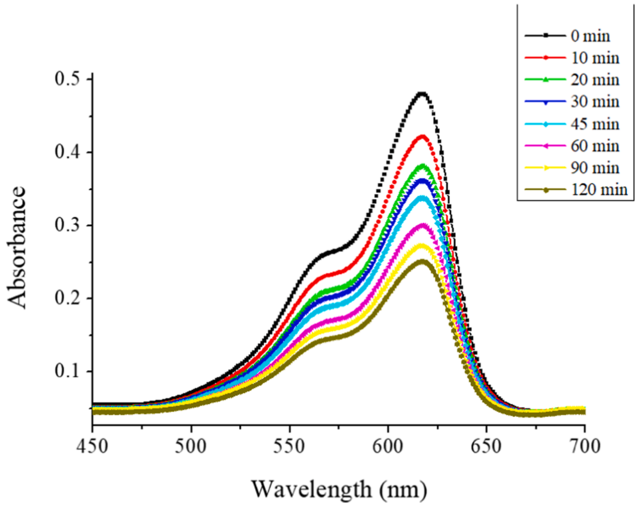

Fig. 14. Malachite Green dye absorbance spectra at different photocatalytic reaction times. (For interpretation of the references to colour in this figure legend, the reader is referred to the web version of this article.)

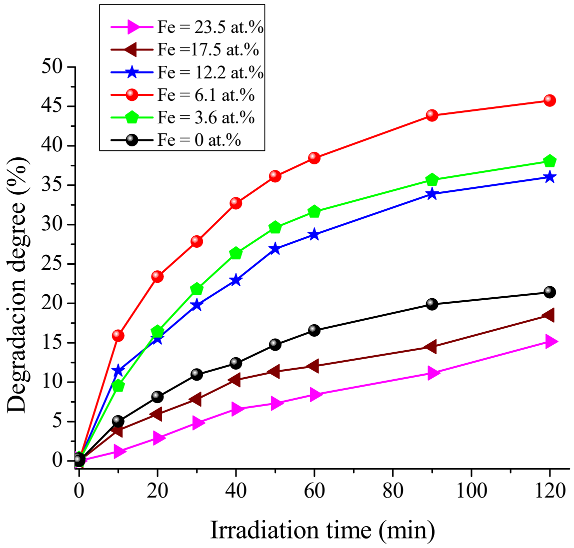

Fig. 15. MG degradation degree as a function of the reaction time for films with different iron content.

to the dye degradation. In contrast, the incorporation of TEOA to the reaction system increases, almost 3 orders of magnitude, the kinetic rate constant, which is explained because the TEOA blocks the holes inhibiting the recombination of the electron-hole pairs, allowing that the electrons can reduce the oxygen dissolved in water producing superoxide radicals increasing the photocatalytic activity. This result indicates that the MG dye degradation is driven by the reduction reaction route, being the main active site the superoxide radicals.

In order to investigate if the found degradation results represent any advantage, they were compared with the degradation values obtained using 5 mg of TiO_2 Degussa P25, a well-known photocatalyst that has a high photoactivity due to the optimization of key parameters such as phase composition, crystallite size, and surface area. Additionally, the reaction rate constant values, k_{app} (min^{-1}) were obtained assuming a pseudo first-order expression and determining the slope of the linear fitting [51]. The obtained values are shown in Fig. 17 where it is clearly seen that the photocatalytic activity of the TiO_2-Fe_2O_3 nanocomposites, with iron contents from 3.6 to 16.2 at.%, becomes substantially higher than the photocatalytic activity of TiO_2 Degussa P25 (horizontal line). Particularly, the sample containing 6.1 at.% shows a reaction rate almost of two times the value of the commercial photocatalyst. These results prove that the prepared photocatalysts under sunlight irradiation are a good option to degrade the MG dye because of the use of 25–33

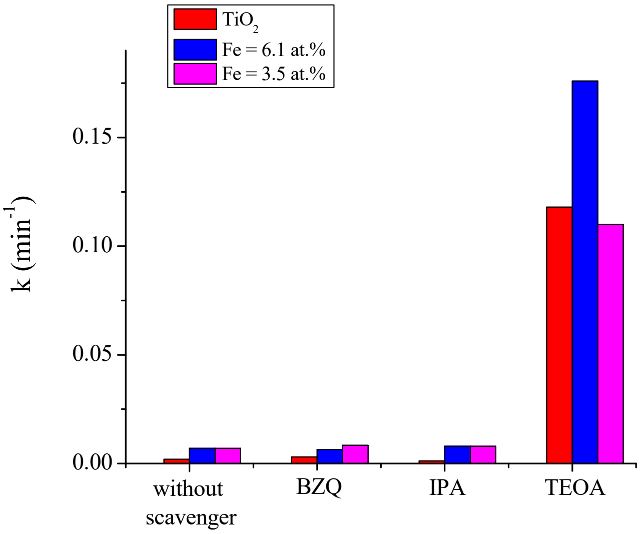

Fig. 16. The kinetic rate constants of the MG degradation reactions in presence of scavenger molecules.

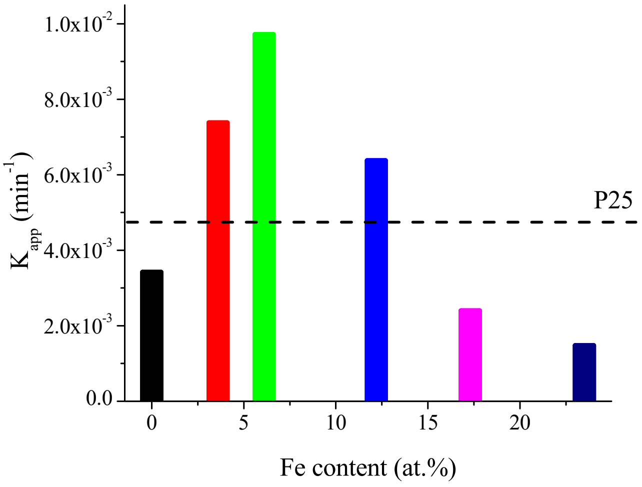

Fig. 17. Reaction rate constant values for films with different Fe content. The value found for the Degussa P25 is included for comparison.

times less mass of photocatalyst and additionally without the problem of the P25 powders recovery.

4. Conclusions

TiO_2-Fe_2O_3 nanocomposite thin films with good photocatalytic response were prepared by magnetron sputtering using a multiple targets configuration. The iron load and the temperature of thermal treatment of the films are key parameters for the physical properties of the obtained materials. Their photocatalytic activity for Malachite Green dye degradation under simulated solar light is found to be higher than TiO_2 and in some cases even better than Degussa P-25 nanopowders. The obtained results suggest that the coupling of these semiconductors results in a higher photocatalytic activity for iron loads of 6.1 at.%. This is confirmed by PL measurements that show an important hindering of the electron–hole pairs recombination at the same Fe load. Finally, it is important to remark that this improved photocatalytic activity was obtained using photocatalysts amounts as low as 150 µgrs.

CRediT authorship contribution statement

L. Escobar-Alarcón: Writing – review & editing, Writing – original draft, Supervision, Methodology, Investigation, Data curation. **D.A. Solis-Casados:** Writing – review & editing, Methodology, Investigation, Data curation. **S. Romero:** Writing – review & editing, Investigation, Data curation. **E. Haro-Poniatowski:** Writing – review & editing, Methodology, Investigation, Data curation.

Declaration of competing interest

The authors declare that they have no known competing financial interests or personal relationships that could have appeared to influence the work reported in this paper.

Data availability

Data will be made available on request.

Acknowledgements

The authors thanks to Arturo Olalde and Fernando Gonzalez Zavala for their technical support.

References

[1] M.D. Hernández-Alonso, F. Fresno, S. Suárez, J.M. Coronado, Development of alternative photocatalysts to TiO_2: challenges and opportunities, Energy Environ. Sci. 2 (2009) 1231, https://doi.org/10.1039/b907933e.
[2] M. Oluwafunmilola Ola, M. Maroto-Valer, Review of material design and reactor engineering on TiO_2 photocatalysis for CO_2 reduction, J. Photochem. Photobiol. C: Photochem. Rev. 24 (2015) 16, https://doi.org/10.1016/j.jphotochemrev.2015.06.001.
[3] S. Shurbaji, P.T. Huong, T.M. Altahtamouni, Review on the visible light photocatalysis for the decomposition of ciprofloxacin, norfloxacin, tetracyclines, and sulfonamides antibiotics in wastewater, Catalysts 11 (4) (2021) 437, https://doi.org/10.3390/catal11040437.
[4] Y. Yamaguchi, A. Kudo, Visible light responsive photocatalysts developed by substitution with metal cations aiming at artificial photosynthesis, Front. Energy 15 (3) (2021) 568–576, https://doi.org/10.1007/s11708-021-0774-8.
[5] A.B. Djurišić, Y. He, A.M.C. Ng, Visible-light photocatalysts: prospects and challenges, APL Mater. 8 (2020) 030903, https://doi.org/10.1063/1.5140497.
[6] L. Gomathi Devi, S. Girish Kumar, Strategies developed on the modification of titania for visible light response with enhanced interfacial charge transfer process: an overview, Cent. Eur. J. Chem. 9 (6) (2011) 959, https://doi.org/10.2478/s11532-011-0084-9.
[7] O.C. Boon, N.L.Y.M.A. Wahab, A review of ZnO nanoparticles as solar photocatalysts: synthesis, mechanisms and applications, Renew. Sustain. Energy Rev. 81 (2018) 536, https://doi.org/10.1016/j.rser.2017.08.020.
[8] S.u. Ren, R. Bechstein, J. Kibsgaard, R.T. Vanga, F. Besenbacher, High-quality Fe-doped TiO_2 films with superior visible-light performance, J. Mater. Chem. 22 (2012) 23755, https://doi.org/10.1039/C2JM34298G.
[9] N. Kaur, S.K. Shahi, J.S. Shahi, S. Sandhu, R. Sharma, V. Singh, Comprehensive review and future perspectives of efficient N-doped, Fe-doped and (N, Fe)-co-doped titania as visible light active photocatalysts, Vacuum 178 (2020) 109429, https://doi.org/10.1016/j.vacuum.2020.109429.
[10] B. Gilbert, C. Frandsen, E.R. Maxey, D.M. Sherman, Band-gap measurements of bulk and nanoscale hematite by soft x-ray spectroscopy, Phys. Rev. B: Condensed Matter 79 (3) (2009) 035108, https://doi.org/10.1103/PhysRevB.79.035108.
[11] K. Hashimoto, H. Irie, A. Fujishima, TiO_2 photocatalysis: a historical overview and future prospects, Jpn. J. Appl. Phys. 44 (2005) 8269, https://doi.org/10.1143/JJAP.44.8269.
[12] X. Liu, K. Chen, J.-J. Shim, J. Huang, Facile synthesis of porous Fe_2O_3 nanorods and their photocatalytic properties, J. Saudi Chem. Soc. 19 (2015) 479, https://doi.org/10.1016/j.jscs.2015.06.009.
[13] D.A. Wheeler, G. Wang, Y. Ling, Y. Li, J.Z. Zhang, Nanostructured hematite: synthesis, characterization, charge carrier dynamics, and photoelectrochemical properties, Energy Environ. Sci. 5 (2012) 6682, https://doi.org/10.1039/C2EE00001F.
[14] H.H. Mohameda, N.H.A. Alomaira, S. Akhtar, T.E. Youssef, Eco-friendly synthesized α-Fe_2O_3/TiO_2 heterojunction with enhanced visible light photocatalytic activity, J. Photochem. Photobiol. A Chem. 382 (2019) 111951, https://doi.org/10.1016/j.jphotochem.2019.111951.
[15] W. Bootluck, T. Chittrakarn, K. Techato, W. Khongnakorn, Modification of surface α-Fe_2O_3/TiO_2 photocatalyst nanocomposite with enhanced photocatalytic activity by Ar gas plasma treatment for hydrogen evolution, J. Environ. Chem. Eng. 9 (2021) 105660, https://doi.org/10.1016/j.jece.2021.105660.

[16] Q. Mei, F. Zhang, N. Wang, Y. Yang, W.u. Ronglan, W. Wang, TiO2/Fe2O3 heterostructures with enhanced photocatalytic reduction of Cr(IV) under visible light irradiation, RSC Adv. 9 (2019) 22764, https://doi.org/10.1039/c9ra03531a.

[17] M.R. Anil Kumar, B. Abebe, H.P. Nagaswarupa, H.C. Ananda Murthy, C. R. Ravikumar, F.K. Sabir, Enhanced photocatalytic and electrochemical performance of TiO_2-Fe_2O_3 nanocomposite: Its applications in dye decolorization and as supercapacitors, Sci. Rep. 10 (2020), https://doi.org/10.1038/s41598-020-58110-7, 1249.

[18] A.M. Ali, M.A. Sayed, H. Algarni, V. Ganesh, M. Aslam, A.A. Ismail, H.M. El-Bery, Synthesis, characterization and photoelectric properties of Fe2O3 Incorporated TiO2 photocatalyst nanocomposites, Catalysts 11 (2021) 1062, https://doi.org/10.3390/catal11091062.

[19] S.C. Lee, H.O. Lintang, L. Yuliati, High photocatalytic activity of Fe_2O_3/TiO_2 nanocomposites prepared by photodeposition for degradation of 2,4-dichlorophenoxyacetic acid, Beilstein J. Nanotechnol. 8 (2017) 915, https://doi.org/10.3762/bjnano.8.93.

[20] A.E. Amoli, M. Masoumi, M. Sharifzaeh, F. Babaei, G.F. Pasha, Synthesis of TiO_2-Fe_2O_3 nanocomposite for the photocatalytic degradation of Direct Blue 199 and Basic Yellow 28 dyes under visible light irradiation, J. Dispers. Sci. Technol. 44 (2023) 630, https://doi.org/10.1080/01932691.2021.1957924.

[21] R.A. Aziz, I. Sopyan, Recent progress on development of TiO_2 thin film photocatalysts for pollutant removal, Recent Pat. Mater. Sci. 2 (2009) 88, https://doi.org/10.2174/1874465610902020088.

[22] P.J. Kelly, R.D. Arnell, Magnetron sputtering: a review of recent developments and applications, Vacuum 56 (2000) 159, https://doi.org/10.1016/S0042-207X(99)00189-X.

[23] A. Djarri, A. Achour, M.A. Soussou, N. Sobti, S. Achour, Characterization of thin films prepared by co-sputtering iron and titanium precursors and thermal oxidation under air atmosphere, Mater Charact 135 (2018) 139, https://doi.org/10.1016/j.matchar.2017.10.008.

[24] L. Escobar-Alarcón, J. Pérez-Álvarez, D.A. Solís-Casados, S. Enrique Camps, J.-B. Romero, Preparation of Co:TiO_2 thin films by crossed beam pulsed laser deposition, Appl. Phys. A 110 (2013) 909, https://doi.org/10.1007/s00339-012-7195-9.

[25] D. Solís-Casados, L. Escobar-Alarcón, M. Fernández, F. Valencia, Malachite green degradation using Ni_x:TiO_2 thin films, Fuel 110 (2013) 17, https://doi.org/10.1016/j.fuel.2012.10.042.

[26] L. Escobar-Alarcón, D.A. Solís-Casados, S. Romero, J.G. Morales-Mendez, E. Haro-Poniatowski, Preparation of Bi:TiO_2 thin films by an hybrid deposition configuration: pulsed laser deposition and thermal evaporation, Appl. Phys. A 117 (2014) 31, https://doi.org/10.1007/s00339-014-8276-8.

[27] A.S. Lim, A. Atrens, ESCA studies of nitrogen containing stainless steels, Appl. Phys. A 51 (1990) 411, https://doi.org/10.1007/BF00348382.

[28] L. Tery, Barr, An ESCA study of the termination of the passivation of elemental metals, J. Phys. Chem. 82 (1978) 1801, https://doi.org/10.1021/100505a006.

[29] R. Shvab, E. Hryha, L. Nyborg, Surface chemistry of the titanium powder studied by XPS using internal standard reference, Powder Metall. 60 (2016) 42, https://doi.org/10.1080/00325899.2016.1271092.

[30] L. Zhu, L.u. Qipeng, L. Lv, Y. Wang, H.u. Yufeng, Z. Deng, Z. Lou, Y. Hou, F. Teng, Ligand-free rutile and anatase TiO2 nanocrystals as electron extraction layers for high performance inverted polymer solar cells, RSC Adv. 7 (2017) 20084, https://doi.org/10.1039/c7ra00134g.

[31] J. Abad, O. Bohme, E. Román, Dissociative adsorption of NO on TiO2(110) argon ion bombarded surfaces, Surf. Sci. 549 (2004) 134, https://doi.org/10.1016/j.susc.2003.11.031.

[32] B. Siemensmeyer, J.W. Schultze, XPS and UPS studies of gas-phase oxidation, electrochemistry and corrosion behaviour of Ti and Ti5Ta, Surf. Interface Anal. 16 (1990) 309, https://doi.org/10.1002/sia.740160164.

[33] G. Greczynski, L. Hultman, Towards reliable X-ray photoelectron spectroscopy: sputter-damage effects in transition metal borides, carbides, nitrides, and oxides, Appl. Surface Sci. 542 (2021) 148599, https://doi.org/10.1016/j.apsusc.2020.148599.

[34] L. Escobar-Alarcón, F. Gonzalez-Zavala, D.A. Solis-Casados, S. Romero, J. Aspiazu, E. Haro-Poniatowski, Zn-modified TiO_2 thin films deposited by combining plasmas produced by laser ablation and magnetron sputtering, Appl. Phys. A 124 (2018) 358, https://doi.org/10.1007/s00339-018-1770-7.

[35] P. Colombo, M. Guglielmi, S. Enzo, Thermal evolution of Fe_2O_3-TiO_2 sol-gel thin films, J. Eur. Ceram. Soc. 8 (6) (1991) 383, https://doi.org/10.1016/0955-2219(91)90018-U.

[36] P. Warren, Y. Murakami, Phase separation in NiTi-Ni_2TiAl alloy system, Mater. Sci. Eng. A, 223 (1997) 17, doi: 10.1016/S0921-5093(96)10472-X.

[37] E. Haro-Poniatowski, R. Rodríguez Talavera, M. de la Cruz Heredia, O. Cano-Corona, R. Arroyo-Murillo, Crystallization of nanosized titania particles prepared by the sol-gel process, J. Mater. Res. 9(8) (1994) 2102, doi: 10.1557/JMR.1994.2102.

[38] M. Hanesch, Raman spectroscopy of iron oxides and (oxy)hydroxides at low laser power and possible applications in environmental magnetic studies, Geophys. J. Int. 177 (2009) 941, https://doi.org/10.1111/j.1365-246X.2009.04122.x.

[39] D.L.A. de Faria, S. Venaüncio Silva, M.T. de Oliveira, Raman microspectroscopy of some iron oxides and oxyhydroxides, J. Raman Spectrosc. 28 (1998) 873, doi: 10.1002/(SICI)1097-4555(199711)28:11<873::AID-JRS177>3.3.CO;2-B.

[40] I.M. Clegg, N.J. Everall, B. King, H. Melvin, C. Norton, On-line analysis using raman spectroscopy for process control during the manufacture of titanium dioxide, Appl. Spec. 55 (2001) 1138, https://doi.org/10.1366/0003702011953388.

[41] G. Teufer, A.K. Temple, Pseudorutile- a new mineral intermediate between Ilmenite and Rutile in the N Alteration of Ilmenite, Nature 211 (1966) 179, https://doi.org/10.1038/211179b0.

[42] A.M. Goodman, Optical interference method for the approximate determination of refractive index and thickness of a transparent layer, Appl. Opt. 17 (1978) 2779, https://doi.org/10.1364/AO.17.002779.

[43] J. Tauc, R. Grigorovici, Vancu, Optical properties and electronic structure of amorphous germanium, A, Phys. Stat. Sol. 15 (1966) 627, https://doi.org/10.1002/pssb.19660150224.

[44] N.D. Abazović, M.I. Čomor, M.D. Dramićanin, D.J. Jovanović, S.P. Ahrenkiel, J. M. Nedeljković, Photoluminescence of anatase and rutile TiO_2 particles, J. Phys. Chem. B 110 (2006) 25366, https://doi.org/10.1021/jp064454f.

[45] M. Koos, I. Pocsik, J. Erostyak, A. Buzadi, Amorphous carbon luminescence; excitation and emission in a broad energy range, J. Non Cryst. Solids 227–230 (1998) 579, https://doi.org/10.1016/S0022-3093(98)00337-8.

[46] A. Lassoued, B. Dkhil, A. Gadri, S. Ammar, Control of the shape and size of iron oxide (α-Fe2O3) nanoparticles synthesized through the chemical precipitation method, Results Phys. 7 (2017) 3007, https://doi.org/10.1016/j.rinp.2017.07.066.

[47] Q.u. Jing Liqiang, W.B. Yichun, L.i. Shudan, J. Baojiang, F.u. Yang Libin, W. F. Hongganga, S. Jiazhong, Review of photoluminescence performance of nano-sized semiconductor materials and its relationships with photocatalytic activity, Sol. Energy Mater. Sol. Cells 90 (2006) 1773, https://doi.org/10.1016/j.solmat.2005.11.007.

[48] X. Pan, M.-Q. Yang, F.u. Xianzhi, N. Zhang, X.u. Yi-Jun, Defective TiO2 with oxygen vacancies: synthesis, properties and photocatalytic applications, Nanoscale 5 (2013) 3601.

[49] M. Laube, F. Rauch, C. Ottermann, Opedro. Anderson, K. Bange, Density of thin TiO_2 films, Nucl. Instrum. Methods Phys. Res., Sect. B 113 (1996) 288, doi: 10.1016/0168-583X(95)01331-8.

[50] D. Xua, B. Cheng, S. Cao, Y.u. Jiaguo, Enhanced photocatalytic activity and stability of Z-scheme Ag_2CrO_4-GO composite photocatalysts for organic pollutant degradation, Appl. Cat. B: Environ. 164 (2015) 380, https://doi.org/10.1016/j.apcatb.2014.09.051.

[51] G. Lente, Deterministic kinetics in chemistry and systems biology. The dynamics of complex reaction networks, Springer Briefs in Molecular Science, Springer International Publishing, doi: 10.1007/978-3-319-15482-4.